

NOTE

A comparison between unfocused and focused transmit strategies in cardiac strain imaging

To cite this article: Vincent Sayseng *et al* 2020 *Phys. Med. Biol.* **65** 03NT01

View the [article online](#) for updates and enhancements.



NOTE

A comparison between unfocused and focused transmit strategies in cardiac strain imaging

RECEIVED
3 April 2019REVISED
20 September 2019ACCEPTED FOR PUBLICATION
4 October 2019PUBLISHED
24 January 2020Vincent Sayseng¹, Julien Grondin², Rachel A Weber¹ and Elisa Konofagou^{1,2,3}¹ Department of Biomedical Engineering, Columbia University, New York, NY, United States of America² Department of Radiology, Columbia University, New York, NY, United States of America³ Author to whom any correspondence should be addressed.E-mail: ek2191@columbia.edu**Keywords:** cardiac strain imaging, coherent compounding, high frame-rate imaging, transthoracic imaging, ultrasound simulation**Abstract**

Unfocused ultrasound imaging, particularly coherent compounding with diverging waves, is a commonly employed high-frame rate transmit strategy in cardiac strain imaging. However, the accuracy and precision of diverging wave imaging compared to focused-beam transmit approaches in human subjects is unknown. Three transmit strategies—coherent compounding imaging, composite focused imaging with ECG gating and narrow-beams, and focused imaging with wide-beams—were compared in simulation and in transthoracic imaging of healthy human subjects ($n = 7$). The focused narrow-beam sequence estimated radial end-systolic cumulative strains of a simulated left ventricular deformation with $26\% \pm 1.5\%$ and $34\% \pm 1.5\%$ greater accuracy compared with compounding and wide-beam imaging, respectively. Strain estimation precision in transthoracic imaging was then assessed with the Strain Filter on cumulative end-systolic radial strains. Within the strain values where statistically significant differences in precision ($E(\text{SNR}_e|\epsilon)$) were found between transmit strategies, the narrow-beam sequence estimated radial strain $13\% \pm 0.71\%$ and $34\% \pm 8.9\%$ more precisely on average compared to compounding or wide-beam imaging, respectively.

Introduction

Strain imaging has proven to be a useful tool in assessing myocardial health (D'hooge *et al* 2000, Abraham *et al* 2007, Dandel *et al* 2009, Smiseth *et al* 2016). Myocardial Elastography (Konofagou *et al* 2002, Lee *et al* 2007), a cardiac strain imaging technique developed by our group, is the particular focus of this study; its applications include tracking ischemia progression in canines (Lee *et al* 2011), lesion monitoring during RF ablation in canines and humans (Grondin *et al* 2015, Bunting *et al* 2018), and quantitatively differentiating ischemic from normal patients as validated by nuclear imaging and angiography (Grondin *et al* 2017b).

Although there are a number of different approaches to estimating cardiac strain with ultrasound (Cikes *et al* 2014), it is well understood that accurate strain estimation is contingent on a frame rate higher than those normally used in clinical B-modes (D'hooge *et al* 2000, Konofagou *et al* 2002, Chen *et al* 2009, Bunting *et al* 2014). Composite focused imaging with ECG gating allows for high spatial and temporal resolution at a full field of view: partial views of the myocardium are imaged over multiple heartbeats, and a composite image is generated by combining the sectors at appropriate time-points in accordance with the ECG (Wang *et al* 2008). However, this approach is vulnerable to artifacts such as irregular ventricular rhythms, and cannot be used in subjects unable to maintain a sufficiently long breathhold (~ 7 s). In order to estimate strain with a single cardiac cycle, a partial transmit aperture may be employed, which forms a less-focused and wider beam (Shattuck *et al* 1984, Von Ramm *et al* 1991, Provost *et al* 2011). Focused imaging with wide beams enables full field-of-view imaging with fewer beams compared the composite focused approach. Unfocused imaging with diverging waves is an alternative to these focused transmit approaches. Coherent compounding sets multiple virtual sources behind

the transducer surface, enabling high frame rates (Hansen *et al* 2014, Papadacci *et al* 2014, Porée *et al* 2015, Apostolakis *et al* 2017, Grondin *et al* 2017, Nayak *et al* 2017, Ssayseng *et al* 2018).

Prior reports have compared unfocused and focused transmit approaches. Park *et al* compared plane wave imaging against focused imaging in a simulated phantom, finding that the former offered inferior or equivalent displacement and strain SNR compared to the latter, depending on distance from the focal zone (Park *et al* 2007). Montaldo *et al* compared the resolution, contrast, and SNR of the B-mode images in tissue-mimicking phantoms, finding that plane wave compounding offered comparable performance as focused approaches but at a much higher frame rate (Montaldo *et al* 2009). Verma and Doyley reported that compounded plane wave imaging generated higher axial and lateral SNR_c in simulated and phantom quasi-static elastography compared to a focused sequence employing a transmit and receive subaperture (Verma and Doyley 2017). Grondin *et al* compared compounding against conventional focused imaging in simulation, and found near-equivalent axial, lateral, and radial strain error (Grondin *et al* 2017). However, these studies were limited to simulation or phantom models. Furthermore, to the best of the authors' knowledge, a comparison between diverging wave imaging and focused approaches in human subjects has yet to be performed.

This study aimed to determine the optimal transmit approach for transthoracic parasternal short-axis strain imaging by comparing the radial strain estimation accuracy and precision of three transmit strategies, all previously employed by our group: composite focused imaging with narrow beams (Pernot *et al* 2007), focused imaging with wide beams (Provost *et al* 2011), and coherently compounded diverging wave imaging (Ssayseng *et al* 2018). The transmit sequences were investigated in simulation to compare strain estimation accuracy, and in transthoracic imaging of healthy human subjects to compare strain estimation precision via the Strain Filter. Unlike previous reports, where the low frame rate of conventional focused transmit approaches precluded RF-based strain estimation outside of quasi-static elastography, implementation of ECG gating and widened beams allowed for comparison of strain estimation accuracy and precision against compounding.

Materials and methods

Description of transmit strategies

Simulated and *in vivo* imaging was performed with a phased array (2.5 MHz, 64 elements, 0.32 mm pitch). The transmit parameters employed in simulation and in *in vivo* transthoracic imaging were identical. The three transmit approaches investigated in this study are graphically summarized in figure 1.

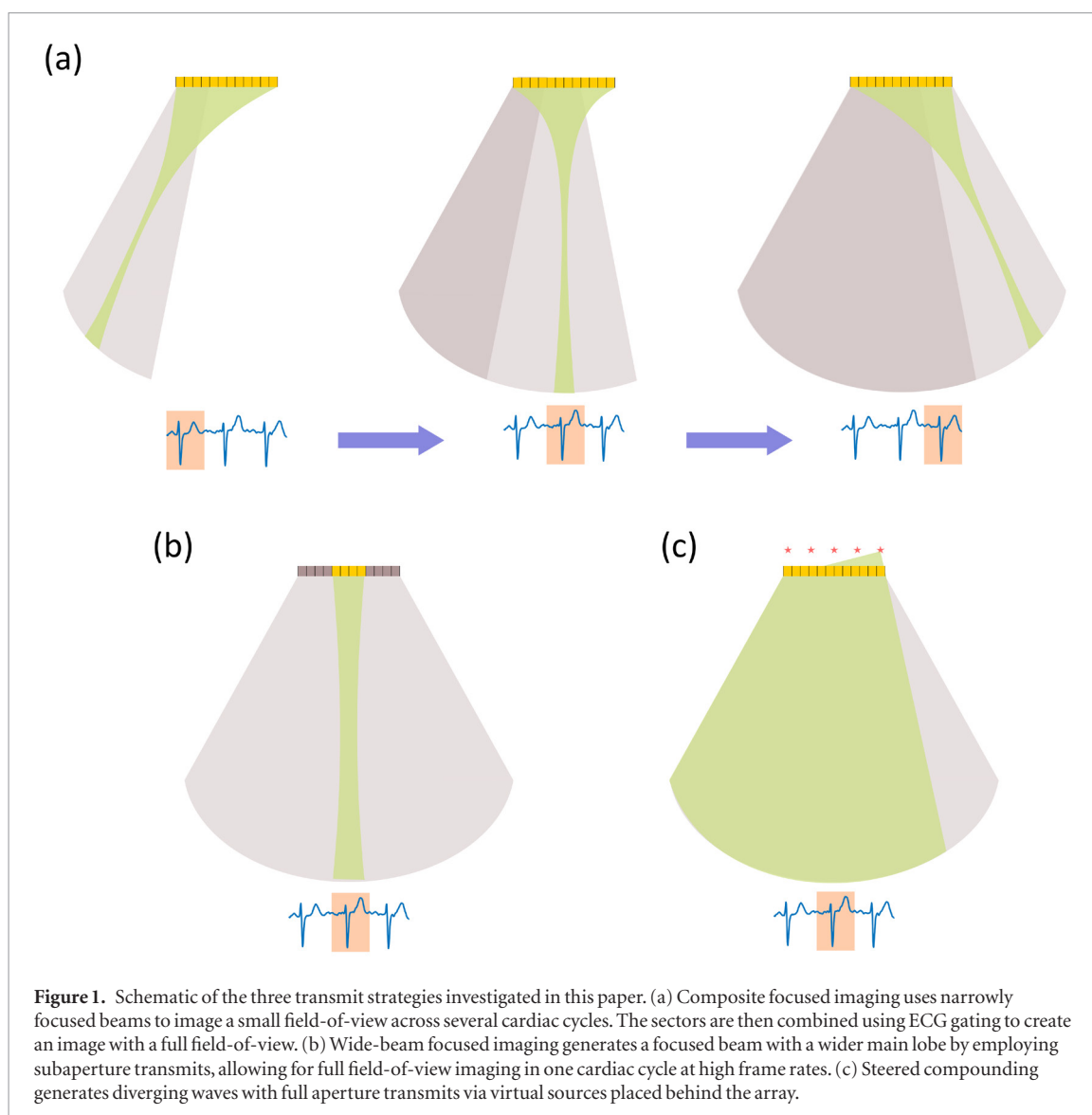
Composite focused imaging with narrow beams and ECG gating entails imaging the heart over multiple cycles to allow for the development of a composite strain image (Wang *et al* 2008). The full-view is divided into sectors that are acquired over different cardiac cycles. ECG gating synchronizes the sectors temporarily with the cardiac cycle, and the patient is required to perform a breathhold to control for translation of the myocardium during the respiratory cycle. A five-sector ECG-gated focused transmit sequence featuring a 75-beam acquisition over a 90° field-of-view at 3000 Hz pulse repetition frequency (PRF) was employed. Axial focal length was set to 60 mm. Beamwidth, defined as the full-width half-maximum (FWHM) of the Field II simulated pressure output at the focus, was 3.7°.

Focused imaging with wide beams uses only a portion of the full transmit aperture (subaperture) to widen the beams. This enables reconstruction of more lines per transmit compared to the ECG gated narrow-beam approach, thus allowing for full field-of-view high frame-rate imaging over one cardiac cycle. A wide-beam sequence featuring a subaperture of 25 elements with 30 transmitted beams over a 90° view at 3000 Hz PRF was employed. Axial focal length was set to 60 mm. The beamwidth was equal to 7.4°, twice that of the ECG-gated focused configuration.

The coherently compounded sequence used diverging waves by setting multiple virtual sources behind the element array. Compounding enables full field-of-view imaging over one cardiac cycle. A full transmit aperture was employed, with steered diverging waves characterized by the number of virtual sources, angular aperture, and tilt angle. A previous study from our group reported that the optimal transmit parameters to maximize strain estimation accuracy and precision in steered compounding at a 3000 Hz PRF were as follows: ten virtual sources, 60° angular aperture, and 15° tilt (Ssayseng *et al* 2018).

Reconstruction of radiofrequency (RF) signals for all three transmit strategies was performed with a delay-and-sum parallel beamformer as described in previous reports (Grondin *et al* 2017b, Ssayseng *et al* 2018). The polar reconstruction grid featured a 90° field-of-view with 180 lines, 77 μm axial sampling, and 14 cm depth. In the ECG-gated focused configuration, two or three reconstructed lines were generated from one transmit beam. In the wide-beam configuration, six reconstructed lines were generated from one transmit beam without overlapping lines.

While all three transmit strategies employed the same PRF (3000 Hz), the motion estimation rate (MER) differed between transmit approaches. PRF is the inverse of the time interval between successive transmits. MER is the inverse of the time interval between successive transmit sets, i.e. the inverse of the time interval between



complete acquisitions used for displacement estimation. A wide-beam set consisted of 30 focused beams; for compounding, a set consisted of ten diverging waves from each virtual source. Consequently, MER for wide-beam and compounding were 100 Hz and 300 Hz respectively. For composite focused imaging, the full field-of-view consisted of five sectors imaged at different cardiac cycles, with 15 focused beams employed for each sector. The resulting MER was thus 200 Hz.

Simulation of left-ventricular contractions

A previously described simulation model in Field II was employed (Sayseng *et al* 2018). Briefly, the left ventricle at end-systole in the parasternal short-axis view was simulated as a symmetrically thickening cylinder (20 mm length, 10 mm thickness) including torsion and out-of-plane displacement: 1.5 mm and 4.5 mm inward radial displacement of the outer and inner walls, respectively; 3.0 mm out-of-plane displacement; and 4° and 8° rotation of the outer and inner walls, respectively. Cumulative radial thickening of the 10 mm thick cylinder was 30% at simulated end-systole. Interframe motion was simulated between each diverging and focused transmit. Systole was simulated over 450 time points, generating 45, 30, and 15 frames of complete acquisitions for the compounding, ECG-gated focused, and wide-beam configurations, respectively. RF data was generated using a simulated cardiac phased array (2.5 MHz, 64 elements, 0.32 mm pitch). Bandlimited noise matching the frequency spectrum of the simulated probe, a P4-2 (ATL/Philips, Andover, MA, USA), was added to the RF signals to simulate decorrelation. Signal magnitude was ten times that of the additive noise. Five trials with unique randomized noise sets were generated to account for potential variability in the strain estimation due to decorrelation.

Axial and lateral displacements were estimated from the beamformed RF signals using a 1D normalized cross-correlation kernel (4.4 mm window, 10% overlap) in a 2D search (Lee *et al* 2007). To increase the accuracy of the lateral estimation, a 10:1 linear interpolation between adjacent RF lines was performed (Konofagou

and Ophir 1998), and a recorrelation method was implemented for three iterations for further refinement (Lee *et al* 2007). Cosine interpolation was applied to achieve subsample displacement estimation (Lee *et al* 2007). A least-squares strain estimator with a window of 3.9 mm by 4° was applied to the accumulated displacements to calculate axial and lateral cumulative strains using the Lagrangian strain tensor (Kallel and Ophir 1997). Radial cumulative strains were then estimated from the 2D strain tensor. Axial, lateral, and radial strain definitions are provided in the appendix. Strains were smoothed with a 4.8 mm by 5.0° median filter.

Strain estimation accuracy was evaluated by comparing the estimated axial, lateral, and radial cumulative strains ($\hat{\varepsilon}$) against the theoretical, end-systolic cumulative strains (ε). Two metrics, absolute and relative error, were implemented to assess accuracy. The absolute strain error, $\delta\hat{\varepsilon}$, was defined as:

$$\delta\hat{\varepsilon}(\%) = \sqrt{(\varepsilon - \hat{\varepsilon})^2}, \quad (1)$$

where ε and $\hat{\varepsilon}$ are theoretical and estimated cumulative strain matrices at end-systole, respectively. $\delta\hat{\varepsilon}$ allows for spatial localization of error.

The relative strain error expressed as a normalized scalar, $\Delta\hat{\varepsilon}$:

$$\Delta\hat{\varepsilon}(\%) = \frac{\sum_{i=1}^n \sqrt{(\varepsilon(i) - \hat{\varepsilon}(i))^2}}{\sum |\varepsilon(i)|} * 100, \quad (2)$$

where ε and $\hat{\varepsilon}$ are n -element theoretical and estimated cumulative strain matrices within the masked region, respectively. The normalized error between transmit strategies for a given cumulative strain type was compared via one-way ANOVA and Tukey multiple comparison procedure in MATLAB (Natick, MA, USA). The mean normalized errors across the five simulated trials was reported.

***In vivo* myocardial imaging**

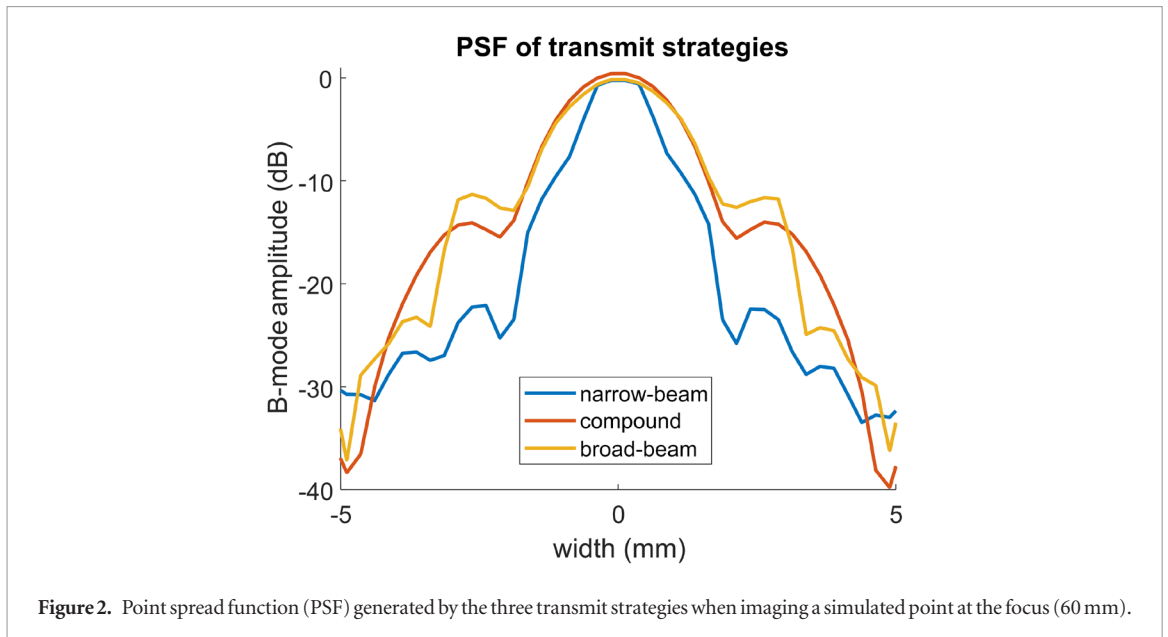
The precision of each transmit strategy was compared via transthoracic imaging of healthy human subjects. The study protocol was conducted with approval from the Institutional Review Board of Columbia University. All three transmit strategies met the FDA limits on acoustic output. Participants were informed of the study's risks, and consent was obtained prior to any imaging. A trained sonographer acquired parasternal short-axis images of the left ventricle at the level of the papillary muscle in seven subjects (25–37 years, male). Images were acquired with an ATL P4-2 phased array probe connected to a research ultrasound system (Verasonics Vantage, Verasonics Redmond, WA, USA). A custom sequence was designed that imaged at 3000 PRF with the following sequences in succession: a 7.5 s focused sequence (75 beams, five sectors), a 1.5 s steered compounding sequence (ten virtual sources, 60° angular aperture, 15° tilt), and a 1.5 s wide-beam sequence (30 beams, one sector). Combining the three transmit strategies within the same sequence ensures that differences in myocardial mechanics were minimal, and that the sonographic view was as consistent as possible between transmit configurations. ECG data was collected in conjunction with the ultrasound acquisition and used to identify systole.

Displacement and strain estimation were performed as described in the previous section. A low motion estimation rate (MER) in the lateral displacement (approximately 100 Hz) was shown to result in a more precise strain estimation (Sayseng *et al* 2018). Consequently, the beamformed RF matrix from the ECG-gated and focused acquisitions was downsampled temporally to a MER of 100 Hz (in the case of the wide-beam sequence, downsampling was not necessary). The resulting lateral displacements were then upsampled to match the original acquisition frame rate to allow calculation of the 2D strain tensor with the axial displacements. Cumulative radial strain was estimated throughout systole. Systole was defined based on the axial displacement through time of the ultrasound line at the center of the myocardium. A mask was manually outlined based on assessment of the B-mode at end-diastole. Only strain values within the mask were used in analysis.

The Strain Filter was used to compare the precision between transmit strategies (Lee *et al* 2007, Bunting *et al* 2014). Elastographic signal-to noise ratio ($\text{SNR}_e = \frac{\mu(\varepsilon)}{\sigma(\varepsilon)}$) measures precision as the ratio of the mean strain to the standard deviation within a small ROI (1.5 mm^2). Translating the SNR_e window throughout the masked area of cumulative strain generates strain- SNR_e pairs. The resulting probability density function (pdf) of SNR_e was normalized to control for strain values that occur more frequently, generating the conditional pdf or $f(\text{SNR}_e|\varepsilon)$. To simplify the 2D conditional pdf, and to more easily compare precision between transmit approaches, expected SNR_e was calculated as

$$E(\text{SNR}_e|\varepsilon) = \int_0^{+\infty} \text{SNR}_e f(\text{SNR}_e|\varepsilon) d\text{SNR}_e. \quad (3)$$

The Strain Filter was used to evaluate end-systolic cumulative radial strains prior to median filtering; that is, the $E(\text{SNR}_e|\varepsilon)$ of the unfiltered strains was reported. In contrast to previous applications of the Strain Filter (Bunting *et al* 2014, Sayseng *et al* 2018), the sign of ε was preserved when calculating $E(\text{SNR}_e|\varepsilon)$. The $E(\text{SNR}_e|\varepsilon)$ of each subject was calculated for the three transmit strategies investigated. The mean $E(\text{SNR}_e|\varepsilon)$ of each transmit



strategy across subjects was statistically compared at each ε bin via a one-way ANOVA and Tukey multiple comparison procedure with MATLAB (2017b, Natick, MA, USA). Graphically, significant ($p < 0.05$) differences in $E(\text{SNR}_c|\varepsilon)$ between transmit strategies for a given value of ε were denoted with a marker.

The strain estimation precision of Myocardial Elastography based on cardiac wall segment was investigated. The mask for a given subject was divided into two segments: an axial segment comprised of the anterior and posterior walls of the myocardium, and a lateral segment comprised of the left lateral and septal walls. The Strain Filter was used to investigate the precision of each segment in measuring *in vivo* radial strain with the focused narrow-beam sequence.

Results

Analysis of simulation

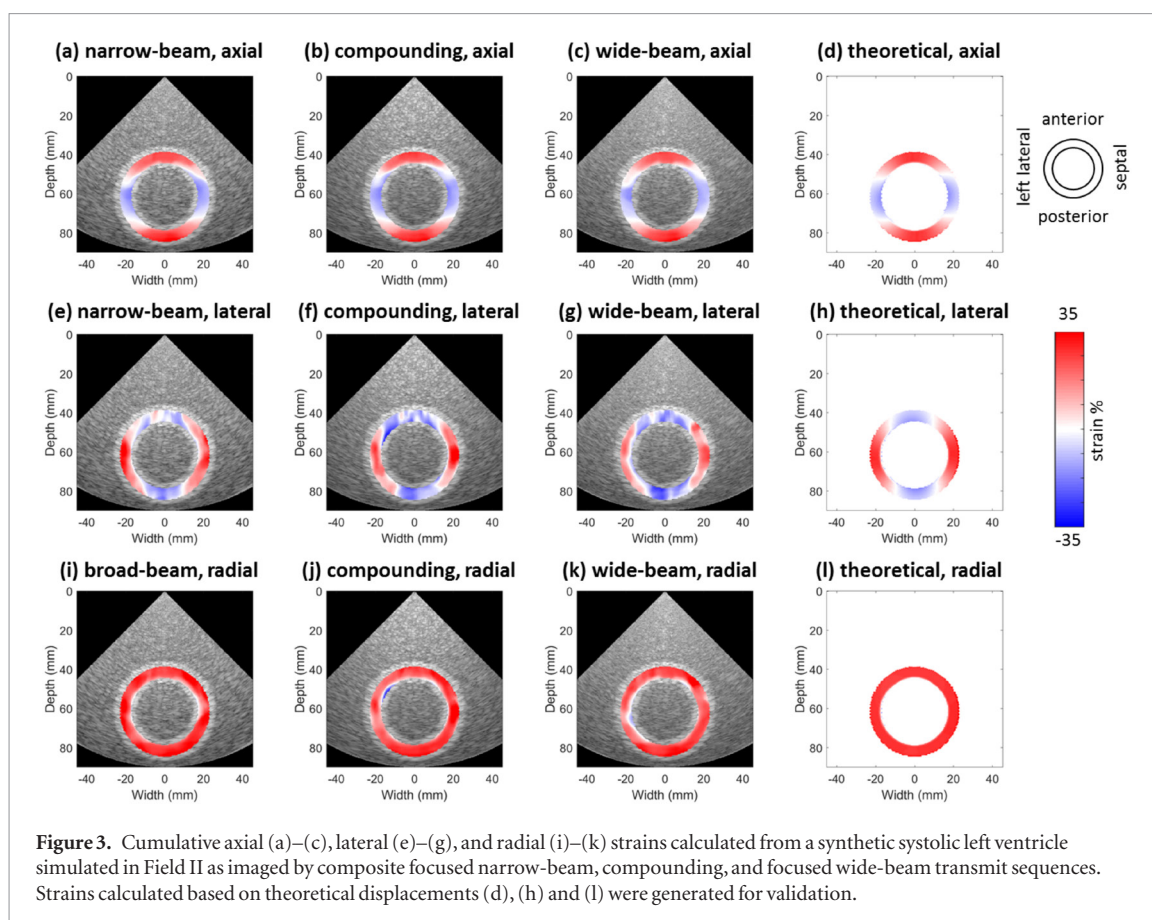
Resolution of the transmit strategies was investigated by imaging a simulated point 60 mm away from the transducer in Field II using the transmit approaches and parameters detailed in the Methods. PSF curves are summarized in figure 2. The width of the principal lobe at -6 dB for the focused narrow-beam, wide-beam, and compounding were 1.4 mm, 2.4 mm, and 2.6 mm, respectively.

The Lagrangian axial, lateral, and radial strains estimated by the transmit strategies are summarized in figure 3. Figure 4 summarizes the spatial distribution of absolute error, $\delta\varepsilon$, in the estimated axial, lateral, and radial strains obtained with each transmit strategy. For all three transmit approaches, the errors in the radial strain estimation are primarily due to the errors in the lateral strain estimate. The accuracy of transmit strategies was further compared using the mean relative error, $\Delta\varepsilon$, across the five simulated trials (figure 5). The focused narrow-beam sequence was the most accurate ($\Delta\varepsilon_{\text{axial}} = 24\%$, $\Delta\varepsilon_{\text{lateral}} = 47\%$, $\Delta\varepsilon_{\text{radial}} = 27\%$), followed by the compounding sequence ($\Delta\varepsilon_{\text{axial}} = 27\%$, $\Delta\varepsilon_{\text{lateral}} = 57\%$, $\Delta\varepsilon_{\text{radial}} = 37\%$), and focused wide-beam sequence ($\Delta\varepsilon_{\text{axial}} = 29\%$, $\Delta\varepsilon_{\text{lateral}} = 67\%$, $\Delta\varepsilon_{\text{radial}} = 42\%$). Strain estimation error was significantly different ($p < 0.001$, Tukey multiple comparison) between the transmit strategies (figure 5). Thus, across the five simulated trials, narrow-beam estimation of radial strain was more accurate by $26\% \pm 1.5\%$ and $34\% \pm 1.5\%$ compared to compounding and wide-beam imaging, respectively. Compounding radial strain estimation had $12\% \pm 2.4\%$ less error relative to wide-beam imaging.

Analysis of transthoracic imaging

The radial strains of one subject imaged with the custom sequence is summarized in figure 6. The radial strain estimated by all three transmit strategies was as expected, showing myocardial thickening over systole (figure 6).

The cumulative radial strains were analyzed quantitatively with the Strain Filter, as summarized in figure 7. The focused narrow-beam sequence performs with the highest precision compared to the compounding and focused wide-beam sequences. Within the strain values where statistically significant differences in the $E(\text{SNR}_c|\varepsilon)$ were found between transmit strategies ($p < 0.05$, Tukey multiple comparison), the narrow-beam sequence estimated radial strain $13\% \pm 0.71\%$ more precisely on average compared to the compounding sequence within the ε range [25%, 40%], and $34\% \pm 8.9\%$ more precisely on average compared to the wide-beam sequence within



the ε range of [4.5%, 60%] (figure 7). The compounding sequence was $23\% \pm 6.6\%$ more precise on average compared to the wide-beam approach in the ε range of [10%, 40%] (figure 7).

Finally, the Strain Filter was used to investigate the precision of the strain estimator in the axial segments (anterior and posterior walls) versus lateral segments (left lateral and septal walls) when using the focused narrow-beam sequence (figure 8). The precision of the axial segments was on average $50\% \pm 14\%$ higher than that of the lateral within the ε ranges of [6.0%, 60%] ($p < 0.05$, Student's t -test).

Discussion

Identification of the transmit strategy that yields the most precise and accurate strain estimation is a critical step in ensuring that ultrasound cardiac strain imaging offers maximum utility in the clinic. The accuracy and precision of strain estimation using composite focused narrow-beam imaging, coherent compounding imaging, and focused wide-beam imaging was determined in simulation and *in vivo* transthoracic imaging. In simulation, it was determined that focused narrow-beam imaging estimates axial, lateral, and radial strain the most accurately, followed by the compounding approach; the focused wide-beam estimation yielded the largest error. *In vivo* quantitative assessment of the strain estimates using the Strain Filter was consistent with the simulation results: the focused narrow-beam approach was the most precise, followed by compounding and then focused wide-beam imaging, respectively.

Analysis of the absolute error maps of the radial (figure 4) strains in simulation clearly demonstrate that the error in the radial strains originates from the lateral estimation; note the similarity in the spatial distribution of error (figures 4(d)–(f) versus figures 4(g)–(i)). In the lateral and radial strain estimates in simulation, error is concentrated in the left lateral and septal walls (figure 4). This observation is corroborated by comparing the relative error of the lateral strain estimation ($\Delta\varepsilon_{\text{lateral,narrow}} = 47\%$, $\Delta\varepsilon_{\text{lateral,compound}} = 57\%$, $\Delta\varepsilon_{\text{lateral,wide}} = 67\%$) with the axial ($\Delta\varepsilon_{\text{axial,narrow}} = 24\%$, $\Delta\varepsilon_{\text{axial,compound}} = 27\%$, $\Delta\varepsilon_{\text{axial,wide}} = 29\%$) (figure 5). Finally, the Strain Filter was used to investigate the precision of the strain estimator in the axial segments (anterior and posterior walls) versus lateral segments (left lateral and septal walls) (figure 8). The precision of the strain estimator in the axial segments was superior to that in the lateral segments, on average $50\% \pm 14\%$ higher within the ε ranges of [6.0%, 60%].

The qualitative differences in the cumulative strains between the transmit strategies both in simulation (figure 3) and in transthoracic imaging (figure 6) were largely subtle. However, the quantitative metrics employed in this paper—absolute (figure 4) and relative (figure 5) error to compare simulated strain estimates, and the Strain

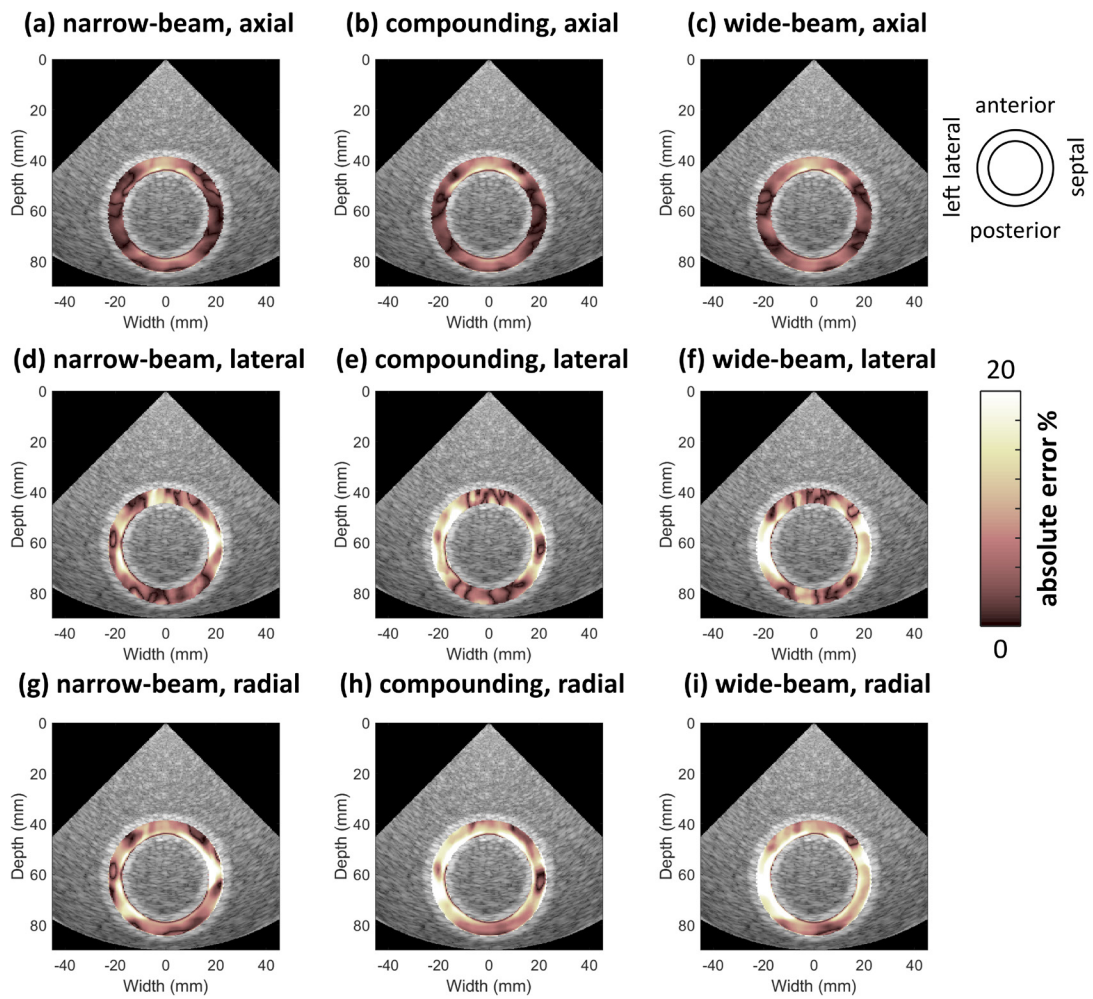


Figure 4. Absolute error ($\delta\epsilon$) in axial (a)–(c), lateral (d)–(f), and radial (g)–(i) strain calculations using composite focused narrow-beam, compounding, and wide-beam transmit sequences to image a simulated systolic left ventricle.

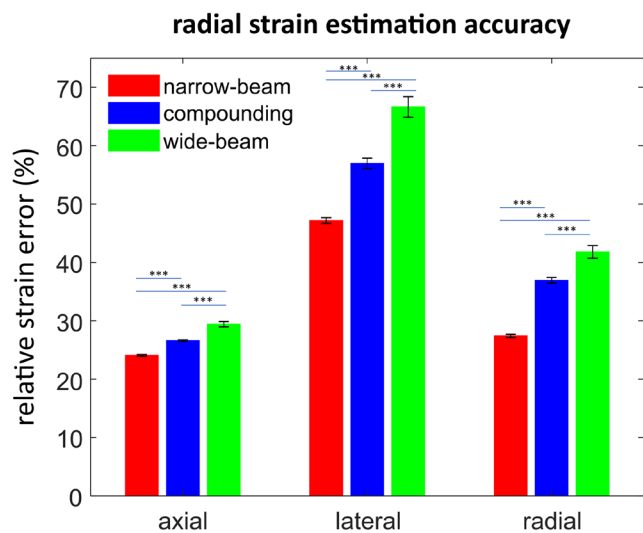
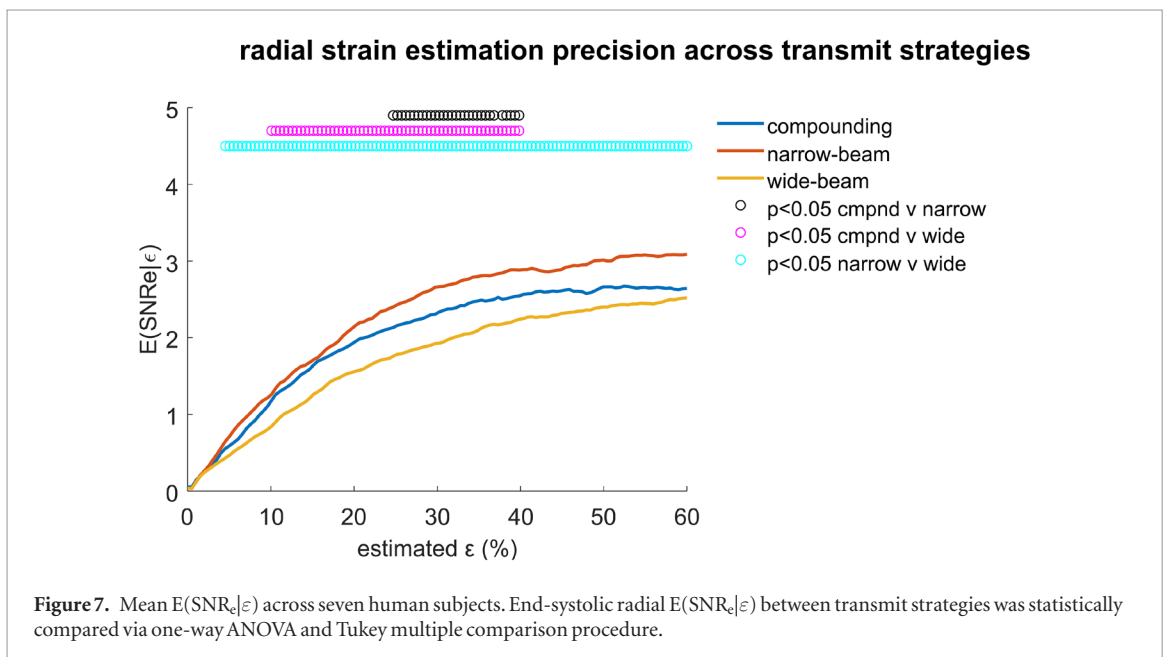
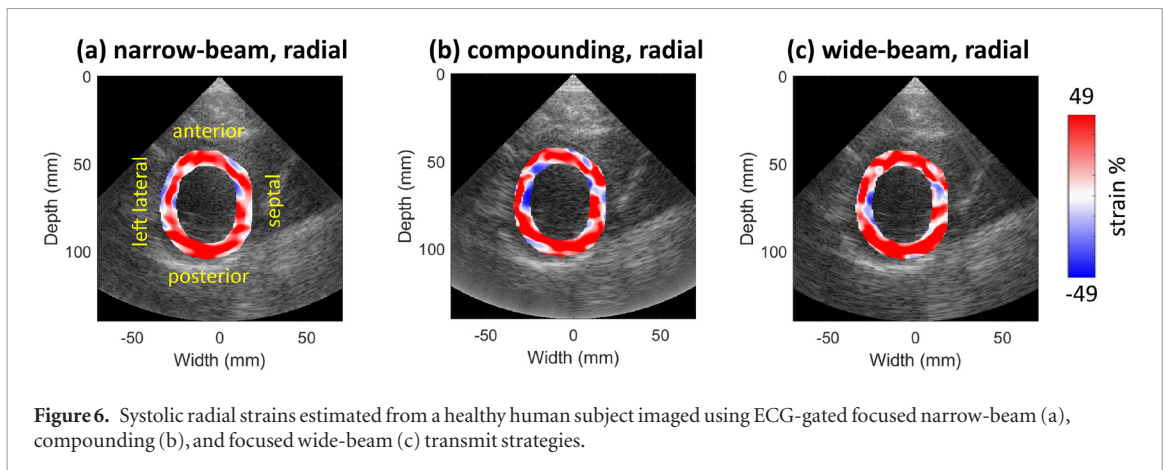


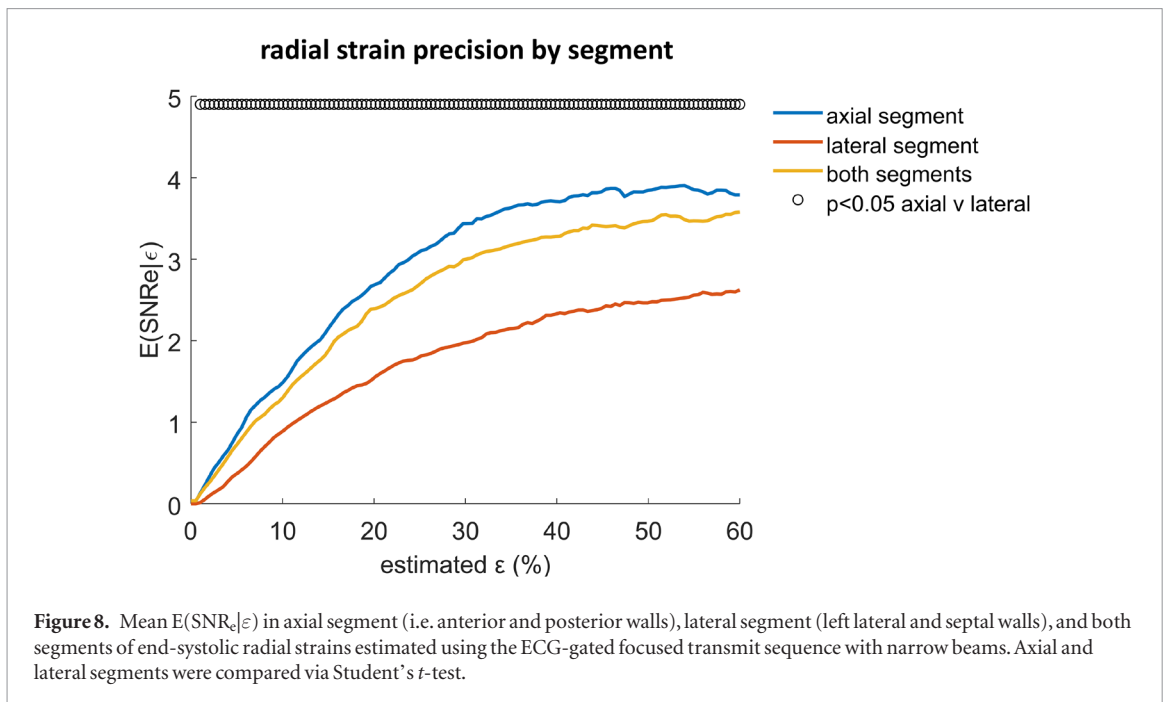
Figure 5. Relative strain error $\Delta\epsilon$ in calculating radial strains using ECG-gated focused narrow-beam, compounding, and focused wide-beam transmit strategies to image a simulated systolic left ventricle. Mean $\Delta\epsilon$ was calculated across five trials. $\Delta\epsilon$ between transmit strategies was statistically compared via one-way ANOVA and Tukey multiple comparison procedure (***) $p < 0.001$.



Filter to examine *in vivo* strains in seven healthy human subjects (figure 7)—were clear in their conclusions that the focused narrow-beam sequence provided the best radial strain estimation in terms of accuracy and precision, followed by the compounding and focused wide-beam approaches, respectively. As summarized in figure 5, narrow-beam imaging estimated radial strain with $26\% \pm 1.5\%$ and $34\% \pm 1.5\%$ less error compared to compounding and wide-beam imaging in simulation, respectively. *In vivo*, figure 7 demonstrates that within the strain range in which statistically significant differences in precision were found between transmit approaches, the focused narrow-beam approach estimated strain $13\% \pm 0.71\%$ and $34\% \pm 8.9\%$ more precisely on average compared to compounding and focused wide-beam imaging, respectively.

The superior performance of the focused narrow-beam sequence may be explained by comparing the PSF generated by each transmit strategy. As summarized in figure 2, the width of the principal lobe at -6 dB was substantially smaller when employing focused narrow-beam imaging (1.4 mm) compared to focused wide-beam or compounding imaging (2.4 and 2.6 mm, respectively). Furthermore, the magnitude of the side lobes generated by the focused narrow-beam sequence are smaller compared to the other two transmit strategies. Based on analysis of the PSF, the focused narrow-beam sequence offers higher resolution and less artifacts from side lobes.

Thus, the focused narrow-beam sequence should be the preferred transmit strategy in patient populations with regular ventricular rhythms that are capable of sustaining a 7.5 s breathhold. A disadvantage of the composite focused approach is that its accuracy and precision is dependent on patient compliance with the breathhold. For patients with irregular ventricular rhythms who are unable to sustain a long breathhold, coherent compounding is the recommended approach. In simulation, compounding estimated strain with $12\% \pm 2.4\%$ more accuracy compared to wide-beam imaging (figure 5). Based on the Strain Filter analysis summarized in figure 7, compounding in transthoracic imaging was $23\% \pm 6.6\%$ more precise on average compared to wide-beam imaging within the ϵ range of [10%, 40%]. Another advantage of compounding is that it has a fifth of the data storage requirements of an ECG-gated focused narrow-beam acquisition.



The focused wide-beam sequence consistently returned the least accurate and least precise strain estimates when compared to the focused narrow-beam and compounding sequences. This may be explained by comparing the MER of the transmit approaches. The focused wide-beam sequence featured the lowest MER of the transmits: 100 Hz, compared to 200 Hz for the focused narrow-beam and 300 Hz for the compounding. The mean of the median correlation coefficient within the masked region through systole and across subjects for the focused narrow-beam, compounding, and focused wide-beam sequences was 0.84, 0.90, and 0.74, respectively. This indicates that the focused wide-beam estimator had the highest levels of decorrelation, while compounding had the least.

The distance from the transducer to the focal spot (or axial focal length) for both the narrow-beam and wide-beam transmit approaches was set to 60 mm in simulation and in imaging patients. The precision and accuracy of the strain estimation is dependent on beamwidth, which is a function of the position of the myocardium relative to the axial focal length (Righetti *et al* 2003, Luo and Konofagou 2009). This relationship was not taken into account in this study and should be the subject of future work.

Conclusion

Selection of the appropriate transmit strategy to implement is integral in optimizing cardiac strain estimation for the clinic. An ECG-gated focused narrow-beam sequence, steered coherently compounded diverging wave sequence, and focused wide-beam sequence were compared in simulation and in transthoracic imaging of healthy subjects to compare the precision and accuracy of each transmit strategy in estimating radial strain. It was shown in simulation that the focused narrow-beam sequence provides the most accurate axial, lateral, and radial strain estimates, with the focused wide-beam sequence providing the least accurate strains. *In vivo* using the Strain Filter, it was shown that the focused narrow-beam sequence measured radial strain with the highest precision, followed by the compounding and wide-beam transmit strategies, respectively.

Funding

This work was supported in part by the National Institutes of Health under Grant R01-EB006042 and R01-HL140646.

Appendix

Previous iterations of Myocardial Elastography have implemented the Lagrangian definition of strain (Lee *et al* 2007). In polar coordinates, the 2D displacement gradient tensor $\nabla \mathbf{u}$ is defined as:

$$\nabla \mathbf{u} = \begin{bmatrix} \frac{\partial u_r}{\partial R} & \frac{1}{R} \frac{\partial u_r}{\partial \Theta} - \frac{u_\Theta}{R} \\ \frac{\partial u_\Theta}{\partial R} & \frac{1}{R} \frac{\partial u_\Theta}{\partial \Theta} + \frac{u_r}{R} \end{bmatrix}, \quad (\text{A.1})$$

where u_θ and u_r are displacements perpendicular and parallel to beam direction, respectively. The displacements were then converted to Cartesian coordinates prior to the strain calculation.

The 2D Lagrangian finite strain tensor \mathbf{E} was defined as:

$$\mathbf{E} = \frac{1}{2}(\nabla\mathbf{u} + (\nabla\mathbf{u})^T + (\nabla\mathbf{u})^T\nabla\mathbf{u}), \quad (\text{A.2})$$

where the diagonal components of \mathbf{E} are the Cartesian lateral (E_{xx}) and axial (E_{yy}) strains. The radial-circumferential strain tensor $\hat{\mathbf{E}}$ may be calculated by applying the rotation matrix $\mathbf{R} = \begin{bmatrix} \cos \Theta & \sin \Theta \\ -\sin \Theta & \cos \Theta \end{bmatrix}$ as follows:

$$\hat{\mathbf{E}} = \mathbf{R}\mathbf{E}\mathbf{R}^T, \quad (\text{A.3})$$

where the diagonal component \hat{E}_{rr} is the radial strain.

ORCID iDs

Vincent Ssayseng  <https://orcid.org/0000-0002-0274-1027>

Julien Grondin  <https://orcid.org/0000-0002-5704-5846>

Elisa Konofagou  <https://orcid.org/0000-0002-9636-7936>

References

- Abraham T P, Dimaano V L and Liang H-Y 2007 Role of tissue Doppler and strain echocardiography in current clinical practice *Circulation* **116** 2597–609
- Apostolakis I Z, McGarry M D J, Bunting E A and Konofagou E E 2017 Pulse wave imaging using coherent compounding in a phantom and *in vivo* *Phys. Med. Biol.* **62** 1700
- Bunting E A, Provost J and Konofagou E E 2014 Stochastic precision analysis of 2D cardiac strain estimation *in vivo* *Phys. Med. Biol.* **59** 6841–58
- Bunting E, Papadacci C, Wan E, Ssayseng V, Grondin J and Konofagou E E 2018 Cardiac lesion mapping *in vivo* using intracardiac myocardial elastography *IEEE Trans. Ultrason. Ferroelectr. Freq. Control* **65** 14–20
- Chen H, Varghese T, Rahko P S and Zagzebski J A 2009 Ultrasound frame rate requirements for cardiac elastography: experimental and *in vivo* results *Ultrasonics* **49** 98–111
- Cikes M, Tong L, Sutherland G R and D'hooge J 2014 Ultrafast cardiac ultrasound imaging: technical principles, applications, and clinical benefits *JACC Cardiovasc. Imaging* **7** 812–23
- D'hooge J, Heimdal A, Jamal F, Kukulski T, Bijnens B, Rademakers F, Hatle L, Suetens P and Sutherland G R 2000 Regional strain and strain rate measurements by cardiac ultrasound: principles, implementation and limitations *Eur. J. Echocardiogr.* **1** 154–70
- Dandel M, Lehmkuhl H, Knosalla C, Suramashvili N and Hetzer R 2009 Strain and strain rate imaging by echocardiography—basic concepts and clinical applicability *Curr. Cardiol. Rev.* **5** 133–48
- Grondin J, Ssayseng V and Konofagou E E 2017 Cardiac strain imaging with coherent compounding of diverging waves *IEEE Trans. Ultrason. Ferroelectr. Freq. Control* **64** 1212–22
- Grondin J, Waase M, Gambhir A, Bunting E, Ssayseng V and Konofagou E E 2017b Evaluation of coronary artery disease using myocardial elastography with diverging wave imaging: validation against myocardial perfusion imaging and coronary angiography *Ultrasound Med. Biol.* **43** 893–902
- Grondin J, Wan E, Gambhir A, Garan H and Konofagou E E 2015 Intracardiac myocardial elastography in canines and humans *in vivo* *IEEE Trans. Ultrason. Ferroelectr. Freq. Control* **62** 337–49
- Hansen H H G, Saris A E C M, Vaka N R, Nillesen M M and de Korte C L 2014 Ultrafast vascular strain compounding using plane wave transmission *J. Biomech.* **47** 815–23
- Kallel F and Ophir J 1997 A least-squares strain estimator for elastography *Ultrason. Imaging* **19** 195–208
- Konofagou E and Ophir J 1998 A new elastographic method for estimation and imaging of lateral displacements, lateral strains, corrected axial strains and poisson's ratios in tissues *Ultrasound Med. Biol.* **24** 1183–99
- Konofagou E E, D'hooge J and Ophir J 2002 Myocardial elastography—a feasibility study *in vivo* *Ultrasound Med. Biol.* **28** 475–82
- Lee W-N, Ingrassia C M, Fung-Kee-Fung S D, Costa K D, Holmes J W and Konofagou E E 2007 Theoretical quality assessment of myocardial elastography with *in vivo* validation *IEEE Trans. Ultrason. Ferroelectr. Freq. Control* **54** 2233–45
- Lee W-N, Provost J, Fujikura K, Wang J and Konofagou E E 2011 *In vivo* study of myocardial elastography under graded ischemia conditions *Phys. Med. Biol.* **56** 1155
- Luo J and Konofagou E E 2009 Effects of various parameters on lateral displacement estimation in ultrasound elastography *Ultrasound Med. Biol.* **35** 1352–66
- Montaldo G, Tanter M, Bercoff J, Benech N and Fink M 2009 Coherent plane-wave compounding for very high frame rate ultrasonography and transient elastography *IEEE Trans. Ultrason. Ferroelectr. Freq. Control* **56** 489–506
- Nayak R, Schifitto G and Dooley M M 2017 Noninvasive carotid artery elastography using multielement synthetic aperture imaging: phantom and *in vivo* evaluation *Med. Phys.* **44** 4068–82
- Papadacci C, Pernot M, Couade M, Fink M and Tanter M 2014 High contrast ultrafast imaging of the human heart *IEEE Trans. Ultrason. Ferroelectr. Freq. Control* **61** 288–301
- Park S, Aglyamov S R, Scott W G and Emelianov S Y 2007 Strain imaging using conventional and ultrafast ultrasound imaging: numerical analysis *IEEE Trans. Ultrason. Ferroelectr. Freq. Control* **54** 987–95
- Pernot M, Fujikura K, Fung-Kee-Fung S D and Konofagou E E 2007 ECG-gated, mechanical and electromechanical wave imaging of cardiovascular tissues *in vivo* *Ultrasound Med. Biol.* **33** 1075–85

- Porée J, Garcia D, Chayer B, Ohayon J and Cloutier G 2015 Noninvasive vascular elastography with plane strain incompressibility assumption using ultrafast coherent compound plane wave imaging *IEEE Trans. Med. Imaging* **34** 2618–31
- Provost J, Nguyen V T-H, Legrand D, Okrasinski S, Costet A, Gambhir A, Garan H and Konofagou E E 2011 Electromechanical wave imaging for arrhythmias *Phys. Med. Biol.* **56** L1–11
- Righetti R, Srinivasan S and Ophir J 2003 Lateral resolution in elastography *Ultrasound Med. Biol.* **29** 695–704
- Sayseng V, Grondin J and Konofagou E E 2018 Optimization of transmit parameters in cardiac strain imaging with full and partial aperture coherent compounding *IEEE Trans. Ultrason. Ferroelectr. Freq. Control* **65** 684–96
- Shattuck D P, Weinshenker M D, Smith S W and von Ramm O T 1984 Explososcan: a parallel processing technique for high speed ultrasound imaging with linear phased arrays *J. Acoust. Soc. Am.* **75** 1273–82
- Smiseth O A, Torp H, Opdahl A, Haugaa K H and Urheim S 2016 Myocardial strain imaging: how useful is it in clinical decision making? *Eur. Heart J.* **37** 1196–207
- Verma P and Doyley M M 2017 Revisiting the cramer rao lower bound for elastography: predicting the performance of axial, lateral and polar strain elastograms *Ultrasound Med. Biol.* **43** 1780–96
- Von Ramm O T, Smith S W and Pavy H G 1991 High-speed ultrasound volumetric imaging system. II. Parallel processing and image display *IEEE Trans. Ultrason. Ferroelectr. Freq. Control* **38** 109–15
- Wang S, Lee W-N, Provost J, Luo J and Konofagou E E 2008 A composite high-frame-rate system for clinical cardiovascular imaging *IEEE Trans. Ultrason. Ferroelectr. Freq. Control* **55** 2221–33